AERODYNAMIC FORCES GENERATED BY AN ELECTROSTATIC INCHWORM MOTOR-ACTUATED MEMS CONTROL SURFACE INTEGRATED ON A FORCE-SENSING PLATFORM

Brian Kilberg, Daniel Contreras, Joseph Greenspun, Hani Gomez, Eric Liu, and Kristofer S. J. Pister*
University of California-Berkeley, Berkeley, California, USA

ABSTRACT

We demonstrate a MEMS-actuated aerodynamic control surface integrated with a piezoresistive force-sensing platform and fabricated in a simple 3-mask silicon-on-insulator (SOI) process. This 47-mg actuator/sensor system generates 0.25 mN of aerodynamic lift force in 23 m/s airflow while operating at 40V, with a rotational displacement of 11 degrees, and a slew rate of 100 degrees/s. This is the first use of an electrostatic inchworm motor to actuate an aerodynamic control surface and generate lift.

INTRODUCTION

Small unmanned aerial systems (sUAS) and micro-air-vehicles (MAVs) have demonstrated useful applications such as search and rescue, aerial photography, crop inspection and biopsy, and industrial chimney inspection [1]–[3]. Scaling these systems down to the pico-air-vehicle (PAV) realm, where dimensions and masses less are than 5 cm and 500 mg, will improve energy consumption, decrease cost, increase ensemble density, and increase data granularity of unmanned aerial systems [3].

Recent advances in mesh networking, MEMS technology, and novel propulsion methods are increasing the feasibility of PAVs [3]. Some of these PAVs include flapping wings, hovering ionocrafts, and potentially ion jet planes [3]–[5]. These vehicles will require millimeter-scale control surfaces in order to control their flight.

Some MEMS control surfaces used arrays of MEMS actuators to manipulate airflow over a centimeter-scale to meter-scale delta wing [6]–[8]. These MEMS arrays aren't suitable for PAVs in their current form because their array size is too large. In [9], Wood et al. developed miniature piezoelectric actuators that were eventually used to actuate the ailerons on a 2 gram microglider [10]. Millimeter-scale control surfaces that are suitable for PAVs will resemble control surfaces like these.

In addition to piezoelectric actuators, electrostatic inchworm motors are also suitable for millimeter-scale control surfaces. Inchworm motors are easy to integrate with transmissions and mechanisms by using simple silicon-on-insulator (SOI) fabrication processes [11]. In MARSS 2017, we reported the design and fabrication of a millimeter-scale MEMS control surface using electrostatic inchworm motors, but did not demonstrate its ability to generate aerodynamic forces [12].

This control surface could be improved by an integrated force measurement system. Integrated force sensing eliminates the need for complicated and cumbersome external force measurement systems, and it enables force feedback applications. Integrated force measurements can be used to improve microbotic control systems. For example, B. Yang et al. used simulated motor force outputs along with machine learning and dynamic simulations of a microrobotic hexapod to design an optimized hexapod gait [13]. Integrated motor force sensors will be necessary in order to evaluate and tune control schemes like these when they are implemented on a physical microrobot.

Several piezoresistive and capacitive force sensors for microrobotic applications have been developed [14]–[16]. The systems in [15] and [16] both were fabricated in an SOI process compatible with an SOI inchworm motor system. Xu et al.

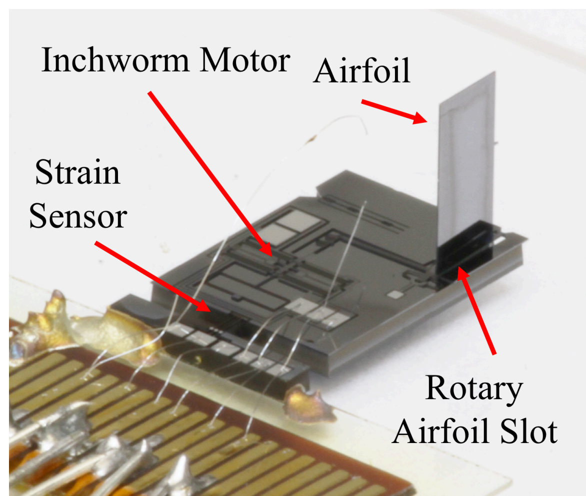

Figure 1: The MEMS control surface consists of an inchworm motor, a 2x4 mm² SOI device layer silicon airfoil, a rotary airfoil slot, and a piezoresistive half-bridge strain sensor. Six wire bonds are used to electrically connect the strain sensor and the motor. The silicon airfoil is inserted into the rotary airfoil slot and stands vertically out of plane from the rest of the device. The strain sensor measures generated lift force.

integrated a capacitive force sensor with an electrostatically-actuated microgripper, which demonstrated the integration of force sensors with actuator systems in SOI processes [17].

This paper describes the design of a MEMS control surface actuation system integrated into a piezoresistive force sensor using a simple SOI process. The SOI process included a 550 μm single-crystal silicon (SCS) substrate, a 2 μm oxide layer, a 40 μm SCS device layer, and a metallization layer. The process steps were a substrate deep reactive ion etch (DRIE), a device-layer DRIE, a metal deposition, and a sacrificial oxide etch.

THEORY AND DESIGN

Aerodynamics and Airfoil Design

Most aircraft use control surfaces such as ailerons, elevons, and rudders to control their trajectories. For thin airfoil theory, where F_l is lift force, ρ is the density of air, V is airflow velocity, C_l is the lift coefficient of the airfoil, A is airfoil area, and α is the angle attack of the airfoil [18]:

$$F_l = \frac{1}{2}\rho V^2 2\pi\alpha A$$

The control surface uses inchworm motors and rotational linkages to rotate a 2x4 mm² device-layer silicon airfoil to change its angle of attack [12]. The airfoil is fabricated in 40-micron thick device layer silicon using the SOI process. As a result of the airfoil's aspect ratio, thin airfoil theory should be an appropriate model. The estimated lift force generated at 23 m/s is 2.8 mN.

Previous simulations showed that control surfaces generating ~10 mN of lift force are sufficient for controlling a millimeter-scale

rocket [3].

MEMS Mechanism

The MEMS control surface consists of electrostatic inchworm motors and rotary joints to actuate a rotary airfoil slot (Figure 2), which are fabricated in the 40-um device layer.

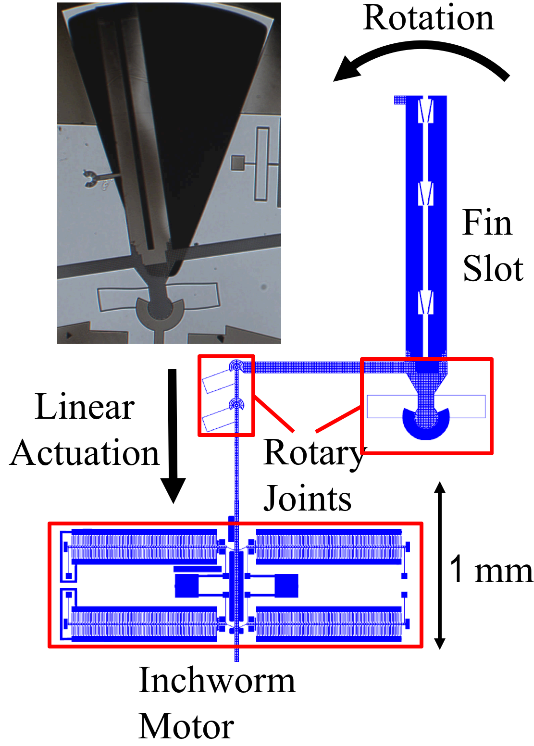

Figure 2: The inchworm motor linearly actuates the rotary joint mechanism which rotates the airfoil slot. The inset shows a microscopic photograph of the airfoil slot after rotation.

In the previous design iteration of this device, airfoil assembly was a significant challenge and decreased the yield of the device assembly process. A self-aligning airfoil slot was designed to avoid this problem. Instead of inserting the fin into the slot from above, the fin is inserted form the side, while spring-loaded mechanisms align and secure the airfoil (Figure 3). A small amount of epoxy was used to permanently fasten the airfoil into the slot. This improvement decreased the failure rate of this assembly step to zero.

Integrated Force-Sensing Platform

The motor, mechanism, and airfoil are fabricated into a platform that has integrated SOI half-bridge strain gauges (Figure 4). When aerodynamic forces are applied to the airfoil, the strain sensor beam deflects and the strain gauge registers a change in voltage. The integrated force sensing platform allowed us to easily measure the aerodynamic forces generated by the airfoil and could enable force feedback control schemes in future PAVs.

Theoretically, the output voltage of the half-bridge strain gauge is $V_o = G\epsilon_{avg}V_x$ where G is the gauge factor, V_x is the differential bridge voltage, and ϵ_{avg} is the average strain throughout the length each of the gauge's piezoresistors.

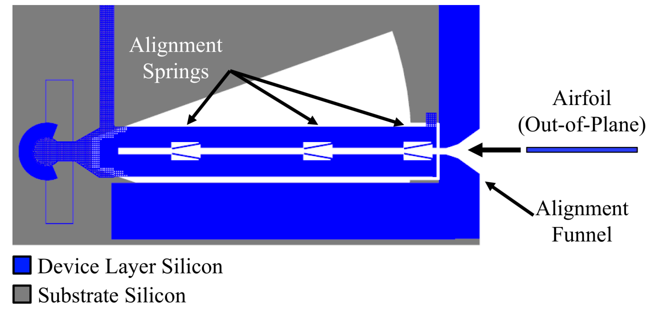

Figure 3: A patterned backside trench underneath the airfoil slot and a device-layer alignment funnel comprise the airfoil alignment mechanism. This mechanism guides the vertically-oriented airfoil into this slot as it is inserted. During airfoil insertion, cantilever springs align and secure the airfoil.

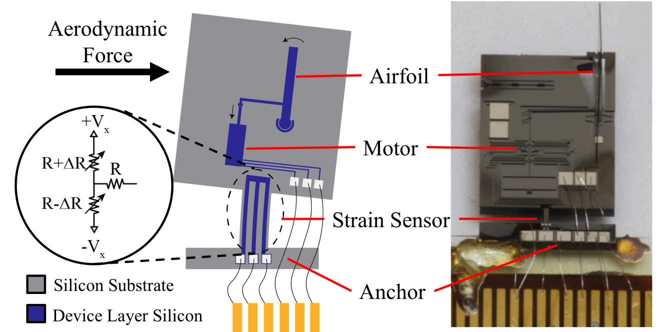

Figure 4: The strain sensor consists of a substrate layer cantilever with device layer piezoresistors patterned on top of the cantilever. When the cantilever deflects, it induces a differential strain in the piezoresistors on the edges of the cantilever. The anchor of the strain sensor is glued to a mount, so the rest of the device is suspended. When the airfoil rotates in airflow, it generates an aerodynamic lift force that deflects the strain sensor.

The gauge factor for 10-20 Ω-cm p-type silicon in the [110] direction, is approximately 120 [19]. The location of the aerodynamic point force and the calibration weight point is offset from the end of the strain sensor beam, which introduces a moment in addition to a load at the end of the beam. The following equation shows the relationship between force applied to the airfoil and the average strain in the piezoresistors of the strain gauge, where F_l is the load force, d is the distance between the neutral axis of the substrate beam and the piezoresistor, L_g is the length of the L_f is the distance between the point where the load force is applied by the airfoil and calibration weights and the end of the beam, E is the Young's modulus of silicon, and I is the moment of inertia of the beam:

$$\epsilon_{avg} = \frac{F_l d(L_f + \frac{L_g}{2})}{EI}$$

With V_x=1.63 V this calculation predicts that the strain sensor will have a scale factor of 1.5 mV/mN.

The strain sensor was calibrated by using known weights to apply force to the sensor and its output was measured through an 1000x amplifier. V_x was 1.64 V. Linear regression was performed on the calibration data, which yielded a linear fit with a slope of 1.96 V/mN and an R^2 value of 0.986. This scale factor of 1.96 V/mN is 31% greater than the predicted 1.5 V/mN (adjusting for amplification) scale factor, and the average standard deviation of

each measurement was 0.0175 mN.

AERODYNAMIC PERFORMANCE

Aerodynamic Performance of Static Fin

The theoretical performance of the airfoil was compared to actual performance by an experiment where the strain sensor was manually rotated with an attached airfoil. The results of this experiment are in figure 5. Airfoil lift force depended linearly on angle of attack for small angles. Lift force was not quadratically related to airflow speed.

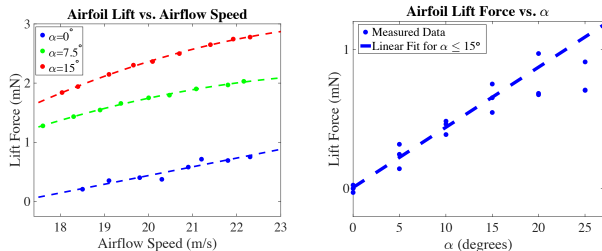

Figure 5: Left and center: Measured relationship between lift force, angle of attack, and airspeed for a 2x4 mm^2 silicon airfoil. In left graph, experiments were run at 15 m/s flow speed. Right: a device with an immobilized airfoil in a wind tunnel was rotated while measuring the lift force.

Active Actuator Aerodynamic Performance

The next experiment measured the amount of aerodynamic force the MEMS control surface could generate while running in airflow. Once placed in 23 m/s airflow, the airfoil was periodically actuated while the strain sensor measured lift force. Figure 6 shows the device setup in this experiment.

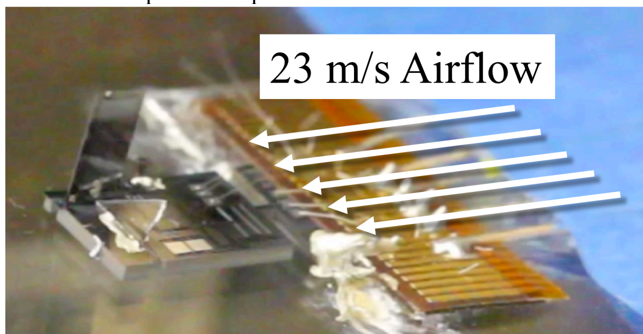

Figure 6: Image of the MEMS control surface system mounted for aerodynamic force experiments.

Low frequency drift was present in the measurement signal, which required signal processing to remove. Force measurements were extracted by comparing force measurements at times when the fin was actuated to times when the fin was at rest (Figure 7). The measured periodic force signature correlated with fin deflection only occurs when both the fin is moving and the control surface is in 23 m/s of airflow, showing that the force measurement is due to aerodynamic force generated by the fin. The average measured lift force was 0.25 mN, which was less than the predicted amount.

SYSTEMS INTEGRATION

Integrated Rocket System

These MEMS control surfaces will be used to create a pencil-sized autonomous rockets. In order to do that, we developed a process to assemble four control surfaces using standard wirebonding techniques and flexible printed circuit boards (PCBs) (Figure 8). Once the control surfaces are mounted on the PCB, it is wrapped around a custom fuselage fabricated by an inkjet 3D printer (Stratasys Objet260 Connex3).

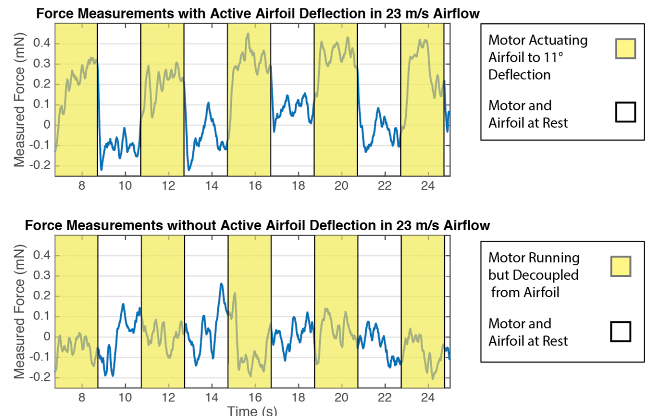

Figure 7: Aerodynamic performance graph. Top: Lift force generated by a periodically actuated airfoil. Noticeable force spikes occur when the fin is rotated by 11 degrees. Bottom: Control experiment showing force exerted on strain sensor when no actuation is occurring in 23 m/s airflow. In this control, the motor is running but is decoupled from the airfoil, so the airfoil doesn't deflect. In both plots, the 4 second moving average was subtracted from the signal

The inchworm motors require 45V – 110V to operate, which poses a power supply challenge at small scales. We designed a portable 90V power supply system using a commercially-available boost-converting integrated circuit (Linear Technologies LT4382), which has a 3mm x 3mm footprint. This system has demonstrated the ability to run a control surface for an hour on a single-cell lithium ion battery. This board was 3.8 cm x 1.5 cm and weighed 2 g. Figure 10 shows an assembled pencil sized rocket including one control surface, battery, and control electronics (Figure 9).

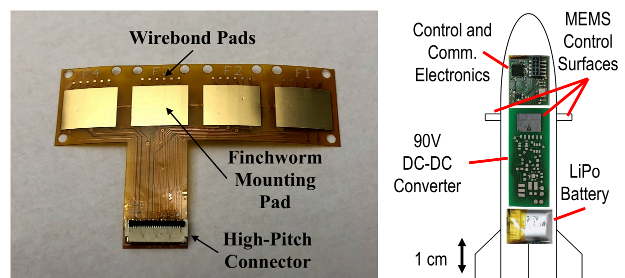

Figure 8: Integrated rocket system components. Left: Flexible PCB designed for assembling and routing control and power signals for the control surface system. The PCB is wrapped around a 3D-printed MEMS control surface fuselage module. Right: All of the electronics necessary to utilize the MEMS control surfaces has been demonstrated in a 1.5 cm diameter body tube.

Island Buckle Joint for Out-of-Plane Stability

Preventing out-of-plane forces from dislocating the silicon mechanisms requires manually glueing a grid of device-layer silicon on top of the rotary pin joint and the securing it with epoxy. This process is laborious and can potentially damage the device beyond repair. In order to avoid this assembly step, we designed a integrated SOI mechanism that prevents out-of-plane dislocation. This

mechanism replaces rotary joint in the control surface. Figure 10 illustrates the operation of this island buckle joint. Inchworm motors were able to rotate the joint to half of the rotation range of the original rotary joint.

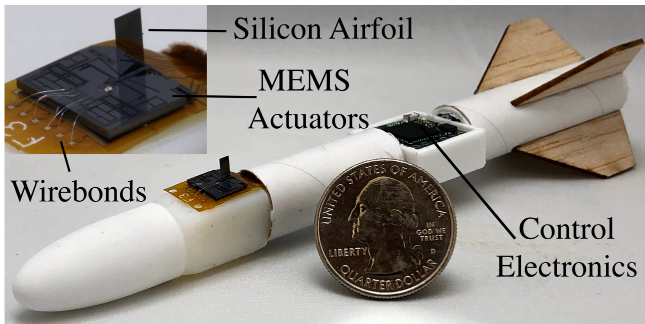

Figure 9: Pencil-sized rocket with one assembled MEMS control surface, LiPo battery, and control electronics attached.

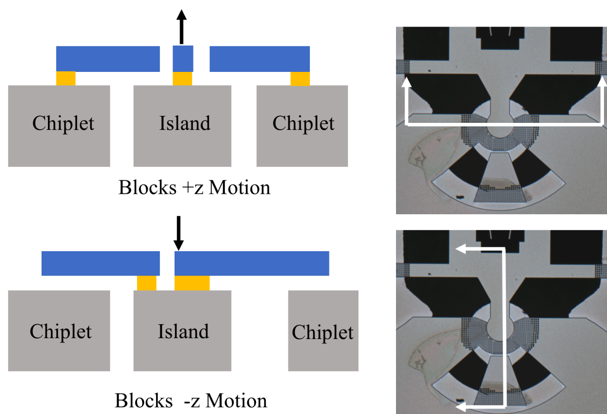

Figure 10: Cross-sections of an island buckle joint illustrate how it prevents out-of-plane dislocations of the device-layer mechanisms. Movement in the positive z direction is constrained by chiplet-anchored cantilevers, while movement in the negative z direction is contained by island-anchored cantilevers.

CONCLUSION

We demonstrated the ability of a MEMS-actuated aerodynamic control surface integrated with a piezoresistive force-sensing platform to generate aerodynamic force up to 0.25 mN. Compared to similar scale piezoelectric control surfaces, this device required 5x lower operating voltage and produced 5x more rotational displacement [10]. The assembly-friendly features added to the control surfaces permit mounting the control surface onto a pencil-sized rocket and will allow for control of the rocket.

REFERENCES

[1] M. Nieuwenhuisen, J. Quenzel, M. Beul, D. Droeschel, S. Houben, and S. Behnke, “ChimneySpector: Autonomous MAV-based indoor chimney inspection employing 3D laser localization and textured surface reconstruction,” *2017 Int. Conf. Unmanned Aircr. Syst. ICUAS 2017*, pp. 278–285, 2017.

[2] D. Orol, J. Das, L. Vacek, I. Orr, M. Paret, C. J. Taylor, and V. Kumar, “An aerial phytobiopsy system: Design, evaluation, and lessons learned,” *2017 Int. Conf. Unmanned Aircr. Syst. ICUAS 2017*, pp. 188–195, 2017.

[3] D. S. Drew, B. Kilberg, and K. S. J. Pister, “Future mesh-networked pico air vehicles,” *2017 Int. Conf. Unmanned Aircr. Syst. ICUAS 2017*, pp. 1075–1082, 2017.

[4] D. S. Drew and K. S. J. Pister, “First takeoff of a flying microrobot with no moving parts,” *Int. Conf. Manip. Autom. Robot. Small Scales, MARSS 2017 - Proc.*, 2017.

[5] K. Y. Ma, P. Chirarattananon, S. B. Fuller, and R. J. Wood, “Controlled flight of a biologically inspired, insect-scale robot,” *Science (80-.).*, vol. 340, no. 6132, pp. 603–607, 2013.

[6] A. Huang, C. Folk, C.-M. Ho, Z. Liu, W. W. Chu, Y. Xu, and Y.-C. Tai, “Gryphon M3 system: integration of MEMS for flight control,” no. October 2001, pp. 85–94, 2001.

[7] C. Folk and C.-M. Ho, “Micro-actuators for control of delta wing with sharp leading edge,” *39th Aerosp. Sci. Meet. Exhib.*, no. January, 2001.

[8] A. Huang, C. Folk, C. Silva, B. Christensen, Y.-F. Chen, G.-B. Lee, M. Chen, S. Newbern, F. Jiang, C. Grosjean, C.-M. Ho, and Y.-C. Tai, “Applications of MEMS devices to delta wing aircraft: From concept development to transonic flight test,” *39th Aerosp. Sci. Meet. Exhib.*, no. January, 2001.

[9] R. J. Wood, E. Steltz, and R. S. Fearing, “Optimal energy density piezoelectric bending actuators,” *Sensors Actuators A Phys.*, vol. 119, no. 2, pp. 476–488, 2005.

[10] R. J. Wood, S. Avadhanula, E. Steltz, M. Seeman, J. Entwistle, A. Bachrach, G. Barrows, S. Sanders, and R. S. Fear, “An autonomous palm-sized gliding micro air vehicle,” *IEEE Robot. Autom. Mag.*, vol. 14, no. 2, pp. 82–91, 2007.

[11] I. Penskiy and S. Bergbreiter, “Optimized electrostatic inchworm motors,” *J. Micromech. Microeng.*, vol. 23, 2013.

[12] B. G. Kilberg, D. S. Contreras, J. Greenspun, and K. S. J. Pister, “MEMS aerodynamic control surfaces for millimeter-scale rockets,” *Int. Conf. Manip. Autom. Robot. Small Scales, MARSS 2017 - Proc.*, 2017.

[13] B. Yang, G. Wang, R. Calandra, D. Contreras, S. Levine, and K. Pister, “Learning Flexible and Reusable Locomotion Primitives for a Microrobot,” pp. 1–8, 2018.

[14] P. Estevez, J. M. Bank, M. Porta, J. Wei, P. M. Sarro, M. Tichem, and U. Staufer, “6 DOF force and torque sensor for micro-manipulation applications,” *Sensors Actuators, A Phys.*, vol. 186, pp. 86–93, 2012.

[15] F. Beyeler, S. Muntwyler, and B. J. Nelson, “Design and calibration of a microfabricated 6-axis force-torque sensor for microrobotic applications,” *Proc. - IEEE Int. Conf. Robot. Autom.*, pp. 520–525, 2009.

[16] W. Zhang, V. T. Truong, K. B. Lua, A. S. Kumar, T. T. Lim, and K. S. Yeo, “Design and characterization of a silicon piezoresistive three-axial force sensor for micro-flapping wing MAV applications,” vol. 9302, no. 65, pp. 1–10, 2015.

[17] Q. Xu, “Design, Fabrication, and Testing of an MEMS Microgripper With Dual-Axis Force Sensor,” *IEEE Sens. J.*, vol. 15, no. 10, pp. 6017–6026, 2015.

[18] G. N. Ward, *Linearized Theory of High-Speed Flow.* Cambridge University Press, 1955.

[19] Y. Kanda, “Piezoresistance effect of silicon,” *Sensors Actuators A. Phys.*, vol. 28, no. 2, pp. 83–91, 1991.

CONTACT

*Brian Kilberg, bkilberg@berkeley.edu